Title: Stress drops on the Blanco oceanic transform fault from inter-station phase coherence.

Joshua R. Williams.
School of Earth and Environment, University of Leeds, Leeds, UK. LS2 9JT.

Jessica C. Hawthorne.
Department of Earth Sciences, University of Oxford, 3 S Parks Rd, Oxford, UK. OX1 3QR.

Sebastian Rost.
School of Earth and Environment, University of Leeds, Leeds, UK. LS2 9JT.

Tim J. Wright.
School of Earth and Environment, University of Leeds, Leeds, UK. LS2 9JT.

Abstract

Oceanic transform faults display a wide range of earthquake stress drops, large aseismic slip, and along-strike variation in seismic coupling. We use and further develop a phase coherence-based method to calculate and analyze stress drops of 61 $M \geq 5.0$ events between 2000 and 2016 on the Blanco Fault, off the coast of Oregon. With this method, we estimate earthquake rupture extents by examining how apparent source time functions (ASTFs) vary between stations. The variation is caused by the generation of seismic waves at different locations along the rupture, which arrive at different times depending on station location. We isolate ASTFs at a range of stations by comparing seismograms of co-located earthquakes and then use the inter-station ASTF coherence to infer rupture extent and stress drop.

We examine how our analysis is influenced by various factors, including poor trace alignment, relative earthquake locations, focal mechanism variation, azimuthal distribution of stations, and depth phase arrivals. We find that as alignment accuracy decreases or distance between earthquakes increases, coherence is reduced, but coherence is unaffected by focal mechanism variation or depth phase arrivals for our dataset. We calibrate the coherence-rupture extent relationship based on the azimuthal distribution of stations.

We find the phase coherence method can be used to estimate stress drops for offshore earthquakes, but is limited to $M \geq 5.0$ earthquakes for the Blanco Fault due to poor trace alignment accuracy. The median stress drop on the Blanco Fault is 8 MPa (with 95% confidence limits of 6-12 MPa) for 61 earthquakes. Stress drops are a factor of 1.7 (95% confidence limits 0.8-3.5) lower on the more aseismic northwest segment of the Blanco Fault. These lower stress drops could be linked to reduced healing time due to higher temperatures, which reduce the depth of the seismogenic zone and shorten the seismic cycle.

Background and Motivation

Oceanic transform faults exhibit a range of slip behaviors that are still poorly understood. They often host large amounts of aseismic slip (e.g., Bird et al., 2002; Boettcher and Jordan, 2004; Materna et al., 2018) and highly repetitive similar ruptures (e.g., Wolfson-Schwehr et al., 2014; Ye et al., 2014). Earthquakes on oceanic transform faults also display a wide variation in stress drops, with both unusually high stress drops (e.g., Allmann and Shearer, 2009; Chen and McGuire, 2016) and some of the lowest recorded stress drops (e.g., Pérez-Campos et al., 2003). Stress drops may also vary between areas with more or less aseismic slip (Moyer et al., 2018). But these behaviors remain poorly understood, as only a modest number of studies have examined earthquake properties on these faults because they are often far from observing stations.

In this study, we add to our knowledge of earthquakes on oceanic transform faults by examining stress drops of offshore earthquakes on the Blanco Fault, an oceanic transform fault off the coast of Oregon, USA (Figure 1). We develop and use a method introduced by Hawthorne et al. (2018), which is a modified form of rupture directivity analysis (e.g., Velasco et al., 1994; Mori, 1996; Somerville et al., 1997; Tan and Helmberger, 2010; Kane et al., 2013). This phase coherence-based method provides an alternative and complementary approach to the commonly used spectral amplitude-based method, as the methods take different approaches to derive rupture extent. With the phase coherence approach, we note that because earthquakes have finite areas, seismic waves are generated at various locations in the rupture and therefore have different travel times to different recording stations. This travel time variation creates differences in the apparent source time functions among the recording stations. We measure differences in apparent source time functions at a range of frequencies, or seismic wavelengths. These measurements allow us to infer the rupture extent and stress drop of an earthquake. In the paper, we determine and take the steps necessary to use this method at long distances.

We use the phase coherence technique to calculate stress drops for M $\geq$ 5.0 earthquakes on the Blanco Fault, offshore of Oregon, USA. We begin by describing the fault, the earthquakes to be considered, and the stations to be used. We then describe the phase coherence method and use it to calculate stress drops. We identify factors that may reduce our coherence, such as inaccurate trace alignment and different earthquake path effects, and only accept results that will not be significantly affected by these factors. Finally, we analyze the acceptable results and discuss their implications for the properties of the Blanco Fault.

Blanco Fault

The Blanco Fault is a right-lateral oceanic transform fault between the Pacific and Juan de Fuca plates. The fault slips at 3 - 8 mm yr^{-1} (Willoughby and Hyndman, 2005) and is split into four transform segments and four topographic depressions (Figure 1) (Dziak et al., 1991; Braunmiller and Nábělek, 2008). The transform segments host mostly strike-slip earthquakes, and the depressions feature normal faulting events (Braunmiller and Nábělek, 2008).

Dziak et al. (1991) noted that the southeastern half of the Blanco Fault, east of the Cascadia Depression (CAS on Figure 1), hosts the largest-magnitude earthquakes and has a higher seismic moment release rate than the northwestern half. They inferred that the southeastern half has less aseismic slip and releases a higher fraction of its moment in earthquakes. Braunmiller and Nábělek (2008) identified a similar large-scale variation in their more detailed investigation. In this study, we will investigate how stress drops vary between the more and less seismic halves of the Blanco Fault.

Earthquake catalog and initial data processing

We initially consider 398 M $\geq$ 4.0 earthquakes that occurred on the Blanco Fault between 2000 and 2016, as identified in the National Earthquake Information Center (NEIC) earthquake catalog. The 398 earthquakes in the catalog are scattered in a 20 - 30 km wide band that follows the fault trace, but shifted northeast of where the fault appears in the bathymetry (Figure 1). This scatter and northeast shift in earthquake locations may be related to uncertainty in arrival time picks and problems with the velocity model, respectively (Dziak et al., 1991; Braunmiller and Nábělek, 2008). Indeed, Kuna et al.

(2019) used high quality OBS data to relocate events on the Blanco Ridge (BLR on Figure 1), and found that the events in 2012 and 2013 relocated onto the bathymetric expression of the fault with very little scatter. We perform our own event relocation later to reduce the effects of the initial location uncertainty on our results.

Earthquakes on the Blanco Fault are recorded by seismic networks along the west coast of North America. We use data from a number of networks, whose data are available via IRIS and the NCEDC (see Data and Resources section). A detailed table of networks used is available in the electronic supplement to this article (Table S1).

We initially consider data from stations within 780 km (7 degrees) of the earthquake locations (Figure 2). We analyze vertical component seismograms from these stations, as we use the first-arriving P-wave. We bandpass filter the seismograms between 0.05 and 20 Hz and pick the P-arrival using a recursive short-term-average/long-term-average algorithm (Withers et al., 1998; Trnkoczy, 1999) in the 1 - 10 Hz frequency band. We discard traces with signal to noise amplitude ratios less than 3 in the 0.5 - 5 Hz frequency band. Further details on data processing are available in the electronic supplement to this article.

Theoretical basis of the phase coherence method

We use the processed data to compute earthquake rupture extents and stress drops. We use a recently developed method (Hawthorne et al., 2018), in which we analyze the similarities and differences of seismograms recorded at various stations. To understand this approach, consider two stations to the south and west (S and W) of an earthquake, as shown in Figure 3. The illustrated earthquake ruptures outward from the hypocenter (black dot) so that its two asperities A (blue) and B (red) rupture simultaneously, but at locations separated by half the rupture diameter D. Asperities A and B are equidistant from the southern station S, so their signals arrive at S at the same time, creating a single peak in the apparent source time function (ASTF). Asperity B is closer to the western station W, so the signal from B arrives at W earlier than the signal from A. This time shift results in two peaks in the ASTF that are separated by time $\frac{1}{2}D/V_P$: by the separation distance divided by the P-wave velocity in the rupture area. In our analysis, we will examine differences in the ASTFs observed at a range of stations to determine how much ASTF peaks could be shifted by intra-source travel time differences. We will use the inferred shifts to estimate the earthquake rupture extents.

However, to analyze ASTFs of real earthquakes, we must first remove the path effects. We use an empirical Green's function approach (similar to, e.g., Dreger et al. 2007; Harrington and Brodsky 2009; Wei et al. 2013; Taira et al. 2014). We note that the seismogram $d_{jk}(t)$ recorded at station k due to earthquake j can be approximated as a convolution of a Green's function $g_k(t)$ and an apparent source time function $s_{jk}(t)$:

$$d_{jk}(t) = s_{jk}(t) \ast g_k(t). \tag{1}$$

Note that we assume that the Green's function retains the same shape across the earthquake rupture area.

If we have two earthquakes ($j = 1$ and $j = 2$) with the same Green's function g_k, then we can eliminate the *phases* of the Green's functions Fourier coefficients by calculating the cross-spectra $\hat{x}_k$ at station k (Hawthorne and Ampuero, 2017):

$$\hat{x}_k = \hat{s}_{1k}\hat{g}_k * \hat{s}_{2k}\hat{g}_k = \hat{s}^*_{1k}\hat{s}_{2k}|\hat{g}_k|^2. \tag{2}$$

Here $\hat{g}_k(\omega)$ is the Fourier transform of $g_k(t)$, $\hat{s}_{jk}(\omega)$ is the Fourier transform of $s_{jk}(t)$, and we have dropped the frequency indexing for readability. Since $\hat{g}_k$ appears in Equation 2 only via its absolute value, the phases of the cross-spectra $\hat{x}_k$ depend only on the relative phases of the earthquakes' ASTFs.

As noted above, we seek to quantify how much the earthquakes' ASTFs vary across stations due to the finite rupture areas. We focus on differences in phase and use a robust estimate of the inter-station similarity: the inter-station phase coherence

$$C_p = \frac{2}{N(N-1)} \sum_{k=1}^{N} \sum_{l=k+1}^{N} \mathrm{Re}\, \frac{\hat{x}_k^* \hat{x}_l}{|\hat{x}_k^* \hat{x}_l|} \tag{3}$$

$$= \frac{2}{N(N-1)} \sum_{k=1}^{N} \sum_{l=k+1}^{N} \mathrm{Re}\, \frac{\hat{s}_{1k} \hat{s}_{1l}^* \hat{s}_{2l} \hat{s}_{2k}^*}{|\hat{s}_{1k} \hat{s}_{1l}^* \hat{s}_{2l} \hat{s}_{2k}^*|}, \tag{4}$$

where there are N stations, and we average coherence over (N-1)*N/2 station pairs. Equation 4 assumes that the two earthquakes have identical Green's functions. With that assumption, C_p provides a measure of the similarity of their ASTFs.

We can compute C_p, and thus the ASTF similarity, for a range of frequencies, or seismic wavelengths. The ASTFs should appear different when the arrival time variation due to the finite rupture extent causes a significant shift in phase. If we consider very long periods, the arrival time variations are a small fraction of the period and thus should not cause a significant shift in phase, so the phases of the ASTFs are similar and C_p is high. At short periods, on the other hand, the travel time variations can be a significant fraction of the period, and thus cause significant shifts in phase and low C_p. The largest travel time variation is proportional to the finite rupture extent of the larger earthquake of the pair, the largest possible distance between generated seismic waves. Therefore, we can calculate the finite rupture extent of the earthquake by identifying the period at which C_p decreases, which should be $F_{scal}D/V_P$: the travel time across the rupture multiplied by a scaling factor F_{scal}.

In order to systematically analyze a range of earthquakes, we define the frequency at which C_p decreases below 0.5 as the falloff frequency f_f. Hawthorne et al. (2018) used synthetics to verify that f_f is inversely proportional to the rupture extent of an earthquake, though they always analyzed groups of earthquakes. In a later section, we analyze a suite of individual earthquake ruptures. We find that given the earthquakes' locations, the iasp91 velocity model (Kennett and Engdahl, 1991), and our land-based station distribution, $f_f = 1.2V_P/D$, where $V_P = 8.04\ km\ s^{-1}$ is the P-wave speed in the oceanic upper mantle.

Once we have estimated f_f and computed rupture extents for a range of earthquakes, we compute their stress drops $\Delta\sigma$. We assume an elliptical slip distribution (Eshelby, 1957) and couple our earthquake rupture radii with moments M_0 obtained from the magnitudes of the NEIC earthquake catalog:

$$\Delta\sigma = \frac{7}{16}\left(\frac{M_0}{\left(\frac{1}{2}D\right)^3}\right). \tag{5}$$

Comparing the phase coherence approach with spectral amplitude analysis

The phase coherence method is sensitive to different earthquake properties than methods that extract corner frequencies from an earthquake's frequency-domain amplitudes (e.g., Shearer et al., 2006; Allmann and Shearer, 2007, 2009). The phase coherence method is most sensitive to the P-wave travel time across the rupture area. It has limited sensitivity to the earthquake's rupture speed and duration (Hawthorne et al., 2018). Spectral amplitude analysis methods, on the other hand, are sensitive to the rupture speed and duration as well as to the P-wave travel time across the rupture area (e.g., Kaneko and Shearer, 2014). In the future, implementing both of these methods may allow us to extract more information about many individual earthquakes: to quickly estimate both the rupture area and the rupture velocity.

Implementing the phase coherence method on the Blanco Fault

Forming earthquake pairs, earthquake relocation, and trace alignment

Before computing stress drops, we must perform a number of processing steps on our data. As a first step, we identify pairs of earthquakes that are potentially closely spaced and could have similar path effects. Since the catalog earthquake locations are uncertain, and scattered in a 20-km wide region around the fault zone, we identify all earthquake pairs which have locations separated by less than 20 km. This identification gives 4636 earthquake pairs, which include 388 unique earthquakes.

Next, we need to align the recordings of these earthquakes. To do so, we relocate the earthquakes in each pair relative to each other using a subset of the seismograms: those with high signal to noise ratios and well-constrained arrival times. To identify the high-quality data, we first bandpass the seismograms between 0.5 and 6 Hz, and cross-correlate a 5-s window beginning on the P-wave arrival to align the traces, removing any traces with a signal to noise power ratio less than 20 in that time window. We then compare the first two seconds of the aligned 5-s windows to assess whether the signals are aligned and similar. We identify the traces that have cross-correlation coefficients larger than 0.6 in the 2-s windows, and extract the relative arrival times from the pairs of seismograms.

We use these arrival times to grid search for the relative earthquake locations. We fix the origin time and location of the higher-magnitude event in each pair and grid search for the best-fitting horizontal location and origin time of the smaller event, with depths fixed at 10 km for both events. For each proposed event location and time, we calculate the predicted P-arrival times using ray tracing (Crotwell et al., 1999) and the 1-D Earth velocity model iasp91 (Kennett and Engdahl, 1991). We compute an L1 norm misfit between the predicted and original estimated differential times from our alignment. In calculating the misfit, we exclude values larger than 0.1 s, as these appear to be due to inaccurate P-arrival picks. We compute the final misfit without these outliers.

We use the location and origin time indicated by the minimum misfit to predict the relative arrival times for all traces, including some that were not used in the locations search. Then we use these times to align the seismograms. We note, however, that some seismograms contain significant noise, so as a final check we compute the cross correlation coefficient for a 2-s window beginning on the P-arrival filtered between 0.5 and 6 Hz. In our stress drop calculations, we use only those seismograms with correlation coefficients higher than 0.6.

This cross correlation coefficient thresholding is important because it allows us to remove noisy traces and to assess whether the path effects are similar - whether we can remove the Green's functions' phases by computing the inter-earthquake phase coherence. But we should note that we have had to use a relatively low cross-correlation threshold compared with some spectral amplitude analysis studies (e.g., Dreger et al., 2007; Abercrombie, 2014, 2015), as we compute the cross-correlation at frequencies that may be above the earthquakes' corner frequencies because the data at lower frequencies is too noisy to use. The low threshold does not seem to strongly affect the results, however, we obtain similar patterns in earthquake stress drops when we use a higher cross-correlation threshold of 0.8, though we obtain stress drops for fewer earthquakes as there are fewer viable stations (see Table S2, Figure S1, and Figure S2 in the electronic supplement to this article). The higher cross-correlation threshold also increases our estimates of median stress drop by roughly 30%.

Calculating the phase coherence

Once we have aligned the traces, we can remove the Green's functions and examine the inter-station ASTF similarity, following the steps outlined in the theoretical basis section. For each earthquake pair, we extract a 5-s window from the aligned traces (Figure 4(a)-(d)) and compute the cross spectra (Equation 2). The phases of some of the cross-spectra for one earthquake pair are shown in Figure 4(e). The cross spectra are similar in the 1 - 3 Hz band, and as expected, the inter-station phase coherence is high in that band (Figure 4(f)). It falls off at higher frequencies, as the cross-spectra phases start to differ. To estimate uncertainties on the coherence, we bootstrap by selecting 1000 subsets of stations with replacement for each earthquake pair. We then calculate the phase coherence for each subset of stations (Equation 4), and derive 95% confidence limits from the overall distribution. The 95% confidence limits are illustrated by the shaded blue area in Figure 4(f).

We follow these steps to calculate coherence as a function of frequency for 1043 earthquake pairs that have more than 10 stations which pass the cross correlation threshold of 0.6. Additional examples of phase coherence profiles and falloff frequency picks are available in the electronic supplement to this article (Figures S3 - S9). For each earthquake pair, we identify the falloff frequency f_f: the frequency at which coherence falls below 0.5, as defined earlier. In identifying f_f, we require that f_f occur at a frequency higher than that of the maximum coherence, because low frequency noise throughout the dataset creates artificially low coherence at low frequencies, which would result in incorrect low falloff frequencies.

Results and Uncertainty assessment

Initial results and uncertainties

We obtain falloff frequencies for 1043 earthquake pairs (22% of our initial earthquake pairs), which include 161 unique events with magnitudes between M $4.2 - 6.0$. We use these falloff frequencies and moments from the earthquake catalog to calculate initial stress drops (Equation 5), and plot the results in Figure 5. When an earthquake is included in multiple pairs, we take the maximum among the pairs as our best estimate of the falloff frequency, since each value can be biased lower than its true value because of poor alignment or spatially varying Green's functions, as discussed later.

In these initial results, the falloff frequency appears to decrease as magnitude increases. Such a decrease is expected, as larger earthquakes typically have larger diameters (e.g., Båth and Duda, 1964; King and Knopoff, 1968; Chinnery, 1969; Kanamori and Anderson, 1975; Wells and Coppersmith, 1994). However, the rate of decrease with magnitude cannot be directly interpreted from these data points, since each falloff frequency estimate could be affected by a range of factors, including (1) incorrect trace alignment, (2) differences in earthquake path effects, (3) differences in focal mechanisms, (4) a limited range of station azimuths, and (5) depth phases in our phase coherence time window. In the following sections, we evaluate how each factor could modify the coherence.

Incorrect trace alignment

The coherence we calculate can be reduced from its true value if the seismograms of the two earthquakes in a pair are poorly aligned. Here we estimate the alignment uncertainty using a loop closure approach. Then we use synthetics to examine how much the alignment error could reduce the inter-earthquake coherence.

To assess the accuracy of our alignment, we consider groups of 3 closely spaced earthquakes and examine the relationships between their arrival times. Consider, for example, the arrival times of three earthquakes at station k: t_{1k}, t_{2k}, and t_{3k}. If these arrival times are correct, then the sum of the relative arrival times, or the loop closure $t_{loop,k}$, should close to zero:

$$t_{loop,k} = (t_{1k} - t_{2k}) - (t_{3k} - t_{2k}) - (t_{1k} - t_{3k}) = 0. \tag{6}$$

We find that 80% of loop closures are within 0.1 s of zero when all 3 events in the loop are within 4 km of each other. Such loop closure accuracy implies that 80% of relative arrival time uncertainties for aligned seismograms are within 0.06 s ($0.1/\sqrt{3}$) of zero. The inferred distribution of arrival time errors is illustrated in the histograms available in the electronic supplement to this article (Figures S10 - S13). Note that we only assess the alignment of earthquakes within 4 km of each other because we will discard results from more widely spaced earthquake pairs in the next section, as they have more variable path effects.

To determine how our alignment uncertainty affects our estimated coherence, we consider the coherence of a template earthquake with itself, after shifting the seismograms by various amounts. We take an earthquake from our dataset and copy its seismograms. Then we pick a set of travel time shifts from the loop closure distribution, apply these shifts to seismograms of the copied event, and calculate the coherence. We repeat this process for 1000 sets of time shifts and use the resulting 1000 coherence profiles to calculate the median phase coherence (black on Figure 6). We find that, on average, the added alignment errors reduce the phase coherence to less than 0.5 at frequencies of 3.7 Hz and above. Note that this frequency threshold is less than 0.2 times the minimum Nyquist frequency (20 Hz) for all but 9 of the 1434 stations we used. Our coherence calculations appear limited by the accuracy of our earthquake relocations, not by the data quality at high frequencies. For further understanding, we also compute the coherence profiles that would be expected if the alignment errors are chosen from various normal distributions. We find that when the alignment error is larger (colored lines on Figure 6), coherence falls off at a lower frequency.

The results above imply that our average alignment uncertainty is likely to reduce perfect coherence ($C_p = 1$) to a coherence of 0.5 by a frequency of 3.7 Hz. Thus when the coherence profiles of real earthquake pairs decrease at frequencies around or above 3.7 Hz, we cannot know whether the falloff in C_p comes from the earthquake's rupture extent or from the average alignment uncertainty. We mark the range of falloff frequencies that are hard to interpret with the green shaded area in Figure 5.

This frequency threshold is especially problematic for smaller earthquakes, which are likely to have higher falloff frequencies. We find in Figure 5 that many $M < 5.0$ earthquakes have falloff frequencies near to or larger than 3.7 Hz. Since those values are hard to interpret, we will exclude $M < 5.0$ events from our discussion and interpretation of

Blanco Fault earthquakes, and we mark $M < 5.0$ in grey on Figure 5.

Differences in earthquake path effects

Another possible bias on falloff frequency comes from earthquake spacing. For our analysis to work, the earthquakes must be co-located so that the path effects will be removed in the cross-spectra calculation for each station. If path effects differ at frequencies lower than the falloff frequency, they will not be removed and we will obtain an apparent falloff frequency that is unrelated to the earthquake's rupture extent, even if each event has similar ASTFs at all stations. Such path effect differences are likely to be larger and more problematic for more widely spaced earthquakes.

We have examined coherence profiles for a number of earthquake pairs with various separations. Examples for a range of inter-earthquake distances are shown in Figure 7. Empirically we find that the coherence profiles remain relatively consistent among earthquake pairs as long as the events are within 4 km of each other. We note, however, that it is difficult to be sure that the path effects are consistent for any pair of earthquakes, so any falloff frequency we estimate should be considered to be a lower bound on the true falloff frequency.

Differences in focal mechanisms

Coherence profiles can also be affected by the focal mechanisms of earthquakes in our pairs. Earthquakes with different focal mechanisms will give rise to different seismograms, even when the earthquakes have the same ASTFs or small rupture areas. Such focal mechanism-induced differences can reduce coherence and result in an incorrect falloff frequency.

Previous analysis of earthquakes on the Blanco Fault suggests that focal mechanisms are unlikely to vary significantly on a 4-km length scale. Braunmiller and Nábělek (2008) observed that strike-slip mechanisms dominate on transform segments of the Blanco Fault, while normal mechanisms are more common within depressions. They found that slip vectors varied by less than 20° along the fault, which suggests that our coherence estimates are unlikely to be reduced due to focal mechanisms.

Limited range of station azimuths

It is not only differences in the earthquakes that can affect the phase coherence, but properties of the station distribution as well. The basis of our method is that we search for ASTF variations caused by varying source-station travel times, which differ due to the stations' azimuths and the rupture directivity (e.g., Mori, 1996; Somerville et al., 1997). However, in our analysis, we have a limited azimuthal distribution of stations; most stations are located at azimuths between 20 and 70° (Figure 2). To determine how this limited azimuthal range could affect our rupture extent estimates, we create synthetic ruptures following the approach of Hawthorne et al. (2018). The synthetic events have heterogeneous slip distributions and rupture bilaterally at velocities of 0.8 times the shear wave speed. We propagate seismic waves due to these ruptures through the iasp91 1-D velocity model (Kennett and Engdahl, 1991). We then compute cross-spectra and phase coherence for these synthetic ruptures. Figure 8 shows the falloff frequencies obtained from synthetic ruptures with a range of diameters. All of these synthetics use the set of stations available for one typical earthquake pair.

The falloff frequencies are roughly 1.2 V_P/D for this station set, where V_P is 8.04 $km\ s^{-1}$, the wavespeed in the oceanic upper mantle, as well as for a few additional representative azimuthal distributions. Note that if we instead assume that stations are randomly distributed on the surface of a homogeneous half space, f_f is 1.1 V_P/D (see Figures S14 - S17 in the electronic supplement to this article).

To understand why the prefactor is higher for our station set, imagine that an earthquake contains two concurrent bursts of slip at either ends of its rupture extent. If those slip bursts are recorded at stations located at 0 and 180° azimuth from the rupture, we would see two peaks in the source time function, where each peak relates to the signal from a slip burst. The time between these peaks is equal to the travel time across the rupture. For stations perpendicular to the rupture, the time between these peaks is approximately zero (see Figure 3 and Figure S18 in the electronic supplement).

In the inter-station phase coherence method, we compute the coherence between station's ASTFs. Stations that are closely spaced have similar arrival times of the slip burst peaks and roughly the same source time function. Stations that are widely spaced have different arrival times of the peaks and thus different source time functions. The maximum difference in arrival times of the peaks that these widely spaced stations can have is the travel time across the rupture. The inter-station coherence thus falls off at a frequency that scales with one over the travel time across the rupture.

With randomly distributed stations, we average the coherence between many widely and closely spaced station pairs and find that coherence falls off at a frequency of 1.1 V_P/D. But for our narrow azimuthal range of stations, we have lots of station pairs that are closely spaced. We find that the coherence falls to 0.5 at a frequency of 1.2 V_P/D, on average. So we assume that the falloff frequency f_f is 1.2 V_P/D when we interpret our f_f in terms of earthquake diameter.

Depth phases in our phase coherence time window

In our coherence analysis, we use a 5-s time window focused on the P-arrival. But other phases, such as the depth phases pP and sP, also arrive in this time window. To assess how the depth phases could affect our coherence, let us consider an earthquake j recorded at stations k, each with a P-arrival followed Δt_{jk} seconds later by a pP-arrival.

If the local earth structure is relatively simple, so that most complexity in the Green's function arises well away from the source, the pP-phase can be approximated as a time-shifted version of the P-arrival, with the same source time function so that the seismogram d_{jk} is (e.g., Letort et al., 2015)

$$d_{jk}(t) = (s_{jk}(t) + Y s_{jk}(t + \Delta t_{jk})) * g_k(t), \tag{7}$$

where Y is a real number that accounts for the reflection coefficient and amplitude of the pP phase, s_{jk} is the ASTF, and g_k is the Green's function of the P-arrival.

When we compute the cross-spectra at a single station k (Equation 2) for a pair of earthquakes ($j = 1$ and $j = 2$), we obtain

$$\hat{x}_k = |\hat{g}_k|^2 (\hat{s}^*_{1k} + Y \hat{s}^*_{1k} e^{-i\omega\Delta t_{1k}})(\hat{s}_{2k} + Y \hat{s}_{2k} e^{i\omega\Delta t_{2k}}) \tag{8}$$

$$= |\hat{g}_k|^2 \hat{s}^*_{1k} \hat{s}_{2k} (1 + Y e^{-i\omega\Delta t_{1k}})(1 + Y e^{i\omega\Delta t_{2k}}). \tag{9}$$

These calculations reveal that the pP-arrival does change the cross spectra; the two terms in parentheses in Equation 9 represent a phase shift for each station resulting from the pP-arrivals for each earthquake, which have different time shifts Δt_{1k} and Δt_{2k}.

In our C_p calculations, however, we are not interested in the phase of any individual $\hat{x}_k$, but in how the time shifts Δt_{jk} are likely to differ among stations. We compute Δt_{jk} using ray tracing and find it is roughly constant (< 0.01 s) for both pP and sP at stations in the 175 - 800 km distance range and for earthquake depths from 0.5 - 20 km (see Figure S19 in the electronic supplement to this article). If Δt_{jk} is consistent across stations k for each event j, then the phase shift of the cross-spectra $\hat{x}_k$ due to the depth phase arrival will also be consistent across stations, and the phase coherence $\hat{x}_k \hat{x}^*_l$ between two stations k and l will be unchanged. Therefore we exclude stations within 175 km of each earthquake before calculating coherence and stress drop, to keep coherence high even if the analyzed time windows include secondary arrivals.

Final stress drop results

In the sections above, we examined how several factors could modify the phase coherence. We (1) assessed resolvable falloff frequencies given the uncertainty in our trace alignment, (2) analyzed how coherence changes with inter-earthquake distance, (3) considered the impact of focal mechanisms, (4) identified appropriate rupture diameter-falloff frequency calibration given the azimuthal distribution of stations, and (5) showed that depth phases are unlikely to influence the coherence in our case. We found that we can identify earthquake pairs with well-resolved coherence by considering only events within 4 km of each other and by noting that falloff frequencies above 3.7 Hz are likely to be unresolvable. This 3.7-Hz resolution limit suggests that we cannot interpret $M < 5.0$ earthquakes due to their high falloff frequencies. After imposing these thresholds, we are left with 298 pairs created from 124 unique events, including 61 M $\geq$ 5.0 earthquakes (see electronic supplement for full results: Figure S20, Table S3). Their falloff frequencies and stress drops are shown in Figure 9.

Analyzing stress drops on the Blanco Fault

Average stress drop

The median stress drop of the 61 M $\geq$ 5.0 earthquakes with well-resolved coherence falloffs is 8 MPa. We compute the uncertainty on the median stress drop by bootstrapping the earthquakes included and by sampling the stress drop probability distributions for individual earthquakes, which we obtained earlier by bootstrapping the stations used (calculating the phase coherence section). For each bootstrap sample, we choose a random subset of the earthquakes with replacement, and recalculate the median using the stress drops picked from the individual earthquakes' probability distributions. We resample 100,000 times and find 95% confidence limits of 6 and 12 MPa on the median stress drop.

The median stress drop for the Blanco Fault found here is higher than values found in some previous studies of oceanic transform faults. Boettcher and Jordan (2004) found values of 0.1 - 0.7 MPa for a global set of faults, and Moyer et al. (2018) found values of 0.03 - 2.7 MPa for the East Pacific Rise transform faults, but our median stress drop is similar to the 6.03 ± 0.68 MPa median stress drop obtained in Allmann and Shearer

(2009)'s global study of oceanic transform faults. However, note that comparing absolute values of stress drops between studies can be prone to error, as different rupture models and analysis methods are used. The difficulty in comparing stress drops between studies means we can only suggest that the median stress drop for the Blanco fault appears to be within an order of magnitude of previous estimates for oceanic transform faults.

In comparing our stress drops with previous results, we also note that the stress drops we calculate here are lower bounds on the true stress drops, because the falloff frequencies are lower bounds on the true falloff frequency. Some of these falloff frequencies may be lower than their true values because of poor trace alignment, or variable Green's functions.

On the other hand, our data limit our ability to examine low stress drop earthquakes. Low frequency noise in the dataset means we cannot identify falloff frequencies below 1 Hz. Indeed, we exclude such earthquakes from our analysis with our initial cross-correlation threshold. The exclusion of low falloff frequency and thus low stress drop earthquakes from our analysis causes us to overestimate the median stress drop.

Note that we include all earthquake pairs in our analysis and do not throw out any earthquake pairs with a small difference in magnitude between them. Tests with synthetic ruptures (see Figure S13 in the electronic supplement to this article) indicate that the falloff frequency is independent of the relative earthquakes' sizes, so long as the ruptures have heterogeneous and different slip distributions. However, any repeating earthquakes with similar slip distributions in the catalog will be assigned inappropriately high falloff frequencies and stress drops with our approach, as such earthquakes could have high coherence at frequencies above the true falloff frequency (Nadeau and Johnson, 1998; Dreger et al., 2007). To check for such a bias, we tried excluding pairs with only 0.1 or 0.2 magnitude unit differences, but the median stress drop and stress drop patterns remain unchanged (see Table S4 in the electronic supplement).

The effects of alignment uncertainty and low frequency noise create a narrow resolution band of falloff frequencies between 1 and 4 Hz. This range of allowed falloff frequencies creates a small apparent increase in stress drop with magnitude in Figure 9. But since that increase is not robust, we do not discuss it further. Most previous studies have found magnitude-independent stress drops (e.g., Abercrombie, 1995; Mori et al., 2003; Shearer et al., 2006; Chen and Shearer, 2011; Uchide et al., 2014; Chen and McGuire, 2016; Abercrombie et al., 2017).

Spatial variation of stress drops

We also examine how stress drops vary with location along the fault. As noted in the Blanco Fault section, Dziak et al. (1991) and Braunmiller and Nábělek (2008) found that the seismic moment release varied along the Blanco Fault, with the northwest segment (west of the Cascadia Depression - see Figure 10) and southeast segment accommodating 3.8% and 14.1% of moment in earthquakes, respectively. We separate the fault into these two segments and calculate median stress drops of the M $\geq$ 5.0 earthquakes on each segment. The 30 M $\geq$ 5.0 events on the NW segment have a median stress drop of 6 MPa (with bootstrap-based uncertainties of 4 to 11 MPa), and the 31 events on the SE segment have a median of 11 MPa (6 to 22 MPa). The two best-fitting median stress drops imply that stress drops on the SE segment are higher by a factor of 1.7, though the 95% confidence intervals allow factors between 0.8 and 3.5.

When interpreting the stress drop ratios, it is important to note that the median stress drops represent averages of individual stress drops that are highly scattered (Figure 10a). Some of the scatter in individual stress drops is likely real inter-earthquake variation which is sampled by our bootstrap-based uncertainty estimate. But some of the scatter is likely an artifact of the analysis method. Our uncertainty estimates account for some of that scatter; we account for noise and station distribution when we create probability distributions for individual earthquakes by bootstrapping the stations included in the analysis. However, there are two sources of bias that we do not account for in our uncertainty estimates. As noted in the last section, our stress drops could be biased low by poor trace alignment or inappropriate empirical Green's functions but the median stress drops could be biased high because we are unable to analyze earthquakes with f_f below 1 Hz. We do find a similar stress drop ratio of 2.1 (with 95% confidence limits of 0.8 and 4.7) using seismograms that passed a cross correlation coefficient threshold of 0.8 as discussed in an earlier section. Those similar ratios suggest that the trace alignment and location scatter are not significantly affecting our results. But we would still urge caution in interpreting the factor of difference we find in this study, due to its high uncertainty.

Despite the uncertainty on our stress drop estimates, it is interesting to note that Moyer et al. (2018) identified a similar spatial variation in stress drops for East Pacific Rise transform faults, where stress drops were a factor of 2 larger in higher seismic moment release areas. They explained their results using the model of Hardebeck and Loveless (2018), where creeping faults had reduced strength and therefore lower stress drops. Another possible explanation for higher stress drops occurring on more seismic segments is that the lower stress drops on the NW segment could arise due to reduced fault healing, related to a shorter seismic cycle and thinner seismogenic zone. Byrnes et al. (2017) identified a negative shear wave velocity anomaly below the NW segment of the Blanco Fault and a positive anomaly beneath the SE segment, which could indicate mantle upwelling beneath the NW segment. The suggested mantle upwelling under the NW segment could lead to a smaller seismogenic zone, and therefore a shallower transition to velocity-strengthening behavior under the NW segment.

The transition to velocity-strengthening frictional sliding and thus to aseismic creep is thought to be temperature dependent, occurring at 500 - 600 °C on transform faults (Abercrombie and Ekström, 2001; Boettcher et al., 2007; He et al., 2007; Braunmiller and Nábělek, 2008). If the temperature of the NW segment is higher due to increased heat flow, aseismic creep will occur at a shallower depth within the fault zone, and the seismogenic zone will be smaller. A smaller seismogenic zone can be loaded more quickly by aseismic slip at depth, and thus is more likely to have a shorter earthquake cycle. The shorter seismic cycle of asperities would allow less time for the fault to heal (Marone et al., 1995; Niemeijer and Spiers, 2006; Hauksson, 2015), and thus reduce its ability to accommodate high stresses. The limited fault strength may allow only lower stress drops on the more aseismic NW segment.

Conclusions

We have demonstrated the applicability of the phase coherence method (Hawthorne et al., 2018) to obtain stress drops for M $\geq$ 5.0 earthquakes on the Blanco Fault. We considered how the coherence estimates are affected by various factors, including incorrect trace alignment, differences in earthquake Green's functions, differences in focal mechanisms, a limited range of station azimuths, and depth phases in our analysis time window. To account for these factors, we first identified the range of falloff frequencies that are resolvable given our alignment uncertainty. We found empirically that differences in Green's functions are minimal for earthquakes within 4 km. We noted that focal mechanisms are unlikely to vary in our data set, and calibrated our rupture diameter estimates to falloff frequency given the azimuthal distribution of stations we have for our events. Finally, we showed that depth phases are unlikely to influence the coherence for oceanic earthquakes observed at distances of several degrees.

Within these constraints, we were able to estimate stress drops of 61 $M \geq 5.0$ earthquakes on the Blanco Fault. Future comparisons of these or other coherence-based stress drops with stress drops derived from spectral amplitude analysis may provide insight into earthquake rupture dynamics and allow us to constrain more earthquake properties, as the various techniques have different sensitivities to the rupture properties and local wavespeeds.

We found a median stress drop of 8 MPa (with 95% confidence limits of 6 to 12 MPa) for the 61 M $\geq$ 5.0 earthquakes on the Blanco Fault with well-resolved coherence falloffs. This median is similar to or higher than other estimates on oceanic transform faults (Boettcher and Jordan, 2004; Allmann and Shearer, 2009; Moyer et al., 2018). The median stress drop is a factor of 1.7 (0.8 to 3.5) higher on the more seismically active southeast segment of the Blanco Fault. This factor of difference should be carefully considered due to the scatter of individual stress drop, and the large uncertainty in the factor itself. Nevertheless, we note that one possible explanation for the lower stress drops on the more aseismic segment, which were also observed on the East Pacific Rise (Moyer et al., 2018), is that the more aseismic segment has higher temperatures, which lead to a shallower seismogenic zone, a shortened seismic cycle, less time for healing and thus less potential for large strength and stress drop in the earthquakes.

Data and Resources

Waveform data, metadata, or data products for this study were accessed through the Northern California Earthquake Data Center (NCEDC), doi:10.7932/NCEDC. Data used in this research were provided by instruments from the Ocean Bottom Seismograph Instrument Pool (http://www.obsip.org) which is funded by the National Science Foundation. OBSIP data are archived at the IRIS Data Management Center (http://www.iris.edu). The facilities of IRIS Data Services, and specifically the IRIS Data Management Center, were used for access to waveforms, related metadata, and/or derived products used in this study. IRIS Data Services are funded through the Seismological Facilities for the Advancement of Geoscience and EarthScope (SAGE) Proposal of the National Science Foundation under Cooperative Agreement EAR-1261681. Waveform data and station metadata for this study were accessed through the Canadian National Data Center (CNDC). Data were processed using Obspy (Beyreuther et al., 2010).

We used data from a number of different seismic networks. These networks include: 5E, 7A, 7D, X9 - Cascadia Initiative (Toomey et al., 2014); BK - Berkeley doi: 10.7932/BDSN; CC - Cascade Chain doi: 10.7914/SN/CC; CN - Canadian National doi: 10.7914/SN/CN; HW - Hanford Washington doi: n/a; LI - LIGO experiment doi: 10.7914/SN/LI; NC - North California doi: 10.7914/SN/NC; NN - Nevada network doi: 10.7914/SN/NN; NV - Neptune Canada doi: n/a; OO - Ocean Observatories Initiative doi: 10.7914/SN/OO; PB - Plate Boundary Borehole doi: n/a; PN - Princeton - Indiana PEPP doi: n/a; PO

- POLARIS doi:n/a; TA - U. S. Array doi: 10.7914/SN/TA; UO - University of Oregon doi: n/a; US - USGS national network doi: 10.7914/SN/US; UW - Pacific Northwest doi: 10.7914/SN/UW; WR - California Water Resources doi: n/a; X1 - Testing Ocean Bottom Seismometer doi: n/a; X4 - Active Fault Mapping doi: 10.7914/SN/X4_2016; XA, XN, ZH - Monitoring asperity on Cascadia megathrust doi: 10.7914/SN/XA_2008, doi: 10.7914/SN/XN_2010, doi: 10.7914/SN/ZH_2011; XD - Mt. St. Helens architecture doi: 10.7914/SN/XD_2014; XG - Cascadia Array of Arrays doi: 10.7914/SN/XG_2009; XH - Cascadia Tremor doi: 10.7914/SN/XH_2004; XT - Western Idaho Shear Zone doi: 10.7914/SN/XT_2011; XU - Earthscope Cascadia project doi: 10.7914/SN/XU_2006; Y3 - Wells, Nevada aftershocks doi: 10.7914/SN/Y3_2008; YG, ZZ - Imaging Cascadian subduction doi: 10.7914/SN/YG_2012, doi: 10.7914/SN/ZZ_2012; YW - Berkeley Cascadian Tremor doi: 10.7914/SN/YW_2007; Z3 - Structure during an ETS event doi: 10.7914/SN/Z3_2009; Z5 - Gorda structure doi: 10.7914/SN/Z5_2013; ZK - Debris flume experiments doi: 10.7914/SN/ZK_2016; and ZU - Glacier quakes on Mt Rainier doi: 10.7914/SN/ZU_2011.

Acknowledgements

Joshua Williams was funded by a studentship from the NERC SPHERES Doctoral Training Partnership (NE/L002574/1). The authors would like to acknowledge Tim Craig for valuable discussion about the physical basis for our variation in stress drops. The authors would also like to thank the two anonymous reviewers for provided useful suggestions to improve on this paper.

References

Abercrombie, R. E. (1995). Earthquake source scaling relationships from- 1 to 5 ML using seismograms recorded at 2.5-km depth, *J. Geophys. Res. B: Solid Earth* **100**(B12), 24015–24036.

Abercrombie, R. E. (2014). Stress drops of repeating earthquakes on the San Andreas fault at Parkfield, *Geophys. Res. Lett.* **41**(24), 8784–8791.

Abercrombie, R. E. (2015). Investigating uncertainties in empirical Green's function analysis of earthquake source parameters, *J. Geophys. Res. B: Solid Earth* **120**(6), 4263–4277.

Abercrombie, R. E., S. Bannister, J. Ristau, and D. Doser (2017). Variability of earthquake stress drop in a subduction setting, the Hikurangi Margin, New Zealand, *Geophys. J. Int.* **208**(1), 306–320.

Abercrombie, R. E. and G. Ekström (2001). Earthquake slip on oceanic transform faults, *Nature* **410**(6824), 74–77.

Allmann, B. P. and P. M. Shearer (2007). Spatial and temporal stress drop variations in small earthquakes near Parkfield, California, *J. Geophys. Res. B: Solid Earth* **112**(B4).

Allmann, B. P. and P. M. Shearer (2009). Global variations of stress drop for moderate to large earthquakes, *J. Geophys. Res. B: Solid Earth* **114**(B1).

Amante, C. and B. Eakins (2009). ETOPO1 1 Arc-Minute Global Relief Model: Procedures, Data Sources and Analysis., *NOAA Technical Memorandum NESDIS NGDC-24.* (National Geophysical Data Center, NOAA.).

Báth, M. and S. J. Duda (1964). Earthquake volume, fault plane area, seismic energy, strain, deformation and related quantities, *Ann. Geophys.* **17**(3), 353–368.

Beyreuther, M., R. Barsch, L. Krischer, T. Megies, Y. Behr, and J. Wassermann (2010, May). ObsPy: A Python Toolbox for Seismology, *Seismol. Res. Lett.* **81**(3), 530–533.

Bird, P., Y. Y. Kagan, and D. D. Jackson (2002). *Plate tectonics and earthquake potential of spreading ridges and oceanic transform faults.* American Geophysical Union.

Boettcher, M. S., G. Hirth, and B. Evans (2007). Olivine friction at the base of oceanic seismogenic zones, *J. Geophys. Res. B: Solid Earth* **112**(B1).

Boettcher, M. S. and T. Jordan (2004). Earthquake scaling relations for mid-ocean ridge transform faults, *J. Geophys. Res. B: Solid Earth* **109**(B12).

Braunmiller, J. and J. Nábělek (2008, July). Segmentation of the Blanco Transform Fault Zone from earthquake analysis: Complex tectonics of an oceanic transform fault, *J. Geophys. Res. B: Solid Earth* **113**(B7).

Byrnes, J. S., D. R. Toomey, E. E. Hooft, J. Nábělek, and J. Braunmiller (2017). Mantle dynamics beneath the discrete and diffuse plate boundaries of the Juan de Fuca plate: Results from Cascadia Initiative body wave tomography, *Geochem. Geophys. Geosyst.* **18**(8), 2906 – 2929.

Chen, X. and J. J. McGuire (2016). Measuring earthquake source parameters in the Mendocino triple junction region using a dense OBS array: Implications for fault strength variations, *Earth Planet. Sci. Lett.* **453**, 276–287.

Chen, X. and P. Shearer (2011). Comprehensive analysis of earthquake source spectra and swarms in the Salton Trough, California, *J. Geophys. Res. B: Solid Earth* **116**(B9).

Chinnery, M. A. (1969). Earthquake magnitude and source parameters, *Bull. Seismol. Soc. Am.* **59**(5), 1969–1982.

Crotwell, H. P., T. J. Owens, and J. Ritsema (1999). The TauP Toolkit: Flexible seismic travel-time and ray-path utilities, *Seismol. Res. Lett.* **70**, 154–160.

Dreger, D., R. M. Nadeau, and A. Chung (2007). Repeating earthquake finite source models: Strong asperities revealed on the San Andreas Fault, *Geophys. Res. Lett.* **34**(23).

Dziak, R. P., C. G. Fox, and R. W. Embley (1991). Relationship between the seismicity and geologic structure of the Blanco Transform Fault Zone, *Mar. Geophys. Res.* **13**(3), 203–208.

Eshelby, J. D. (1957). The determination of the elastic field of an ellipsoidal inclusion, and related problems. In *Proceedings of the Royal Society of London A: Mathematical, Physical and Engineering Sciences*, Volume 241, pp. 376–396. The Royal Society.

Hardebeck, J. L. and J. P. Loveless (2018). Creeping subduction zones are weaker than locked subduction zones, *Nat. Geosci.* **11**(1), 60.

Harrington, R. M. and E. E. Brodsky (2009, August). Source duration scales with magnitude differently for earthquakes on the San Andreas Fault and on secondary faults in Parkfield, California, *Bull. Seismol. Soc. Am.* **99**(4), 2323 – 2334.

Hauksson, E. (2015). Average stress drops of Southern California earthquakes in the context of crustal geophysics: implications for fault zone healing, *Pure Appl. Geophys.* **172**(5), 1359–1370.

Hawthorne, J. and J.-P. Ampuero (2017). A phase coherence approach to identifying co-located earthquakes and tremor, *Geophys. J. Int.* **209**(2), 623–642.

Hawthorne, J. C., A. M. Thomas, and J.-P. Ampuero (2018). The rupture extent of low frequency earthquakes near Parkfield, CA, *Geophys. J. Int.* **216**(1), 621–639.

He, C., Z. Wang, and W. Yao (2007). Frictional sliding of gabbro gouge under hydrothermal conditions, *Tectonophysics* **445**(3-4), 353–362.

Kanamori, H. and D. L. Anderson (1975). Theoretical basis of some empirical relations in seismology, *Bull. Seismol. Soc. Am.* **65**(5), 1073–1095.

Kane, D. L., P. M. Shearer, B. P. Goertz-Allmann, and F. L. Vernon (2013). Rupture directivity of small earthquakes at Parkfield, *J. Geophys. Res. B: Solid Earth* **118**(1), 212–221.

Kaneko, Y. and P. Shearer (2014). Seismic source spectra and estimated stress drop derived from cohesive-zone models of circular subshear rupture, *Geophys. J. Int.* **197**(2), 1002–1015.

Kennett, B. and E. Engdahl (1991). Traveltimes for global earthquake location and phase identification, *Geophys. J. Int.* **105**(2), 429–465.

King, C.-Y. and L. Knopoff (1968). Stress drop in earthquakes, *Bull. Seismol. Soc. Am.* **58**(1), 249–257.

Kuna, V. M., J. L. Nábělek, and J. Braunmiller (2019). Mode of slip and crust–mantle interaction at oceanic transform faults, *Nat. Geosci.* **12**(2), 138 – 142.

Letort, J., J. Guilbert, F. Cotton, I. Bondár, Y. Cano, and J. Vergoz (2015). A new, improved and fully automatic method for teleseismic depth estimation of moderate earthquakes (4.5< M< 5.5): application to the Guerrero subduction zone (Mexico), *Geophys. J. Int.* **201**(3), 1834–1848.

Marone, C., J. E. Vidale, and W. L. Ellsworth (1995). Fault healing inferred from time dependent variations in source properties of repeating earthquakes, *Geophys. Res. Lett.* **22**(22), 3095–3098.

Materna, K., T. Taira, and R. Bürgmann (2018). Aseismic Transform Fault Slip at the Mendocino Triple Junction From Characteristically Repeating Earthquakes, *Geophys. Res. Lett.* **45**(2), 699–707.

Mori, J. (1996). Rupture directivity and slip distribution of the M 4.3 foreshock to the 1992 Joshua Tree earthquake, Southern California, *Bull. Seismol. Soc. Am.* **86**(3), 805–810.

Mori, J., R. E. Abercrombie, and H. Kanamori (2003). Stress drops and radiated energies of aftershocks of the 1994 Northridge, California, earthquake, *J. Geophys. Res. B: Solid Earth* **108**(B11).

Moyer, P. A., M. S. Boettcher, J. J. McGuire, and J. A. Collins (2018). Spatial and Temporal Variations in Earthquake Stress Drop on Gofar Transform Fault, East Pacific Rise: Implications for Fault Strength, *J. Geophys. Res. B: Solid Earth* **123**(9), 7722–7740.

Nadeau, R. M. and L. R. Johnson (1998). Seismological studies at Parkfield VI: Moment release rates and estimates of source parameters for small repeating earthquakes, *Bull. Seismol. Soc. Am.* **88**(3), 790–814.

Niemeijer, A. and C. Spiers (2006). Velocity dependence of strength and healing behaviour in simulated phyllosilicate-bearing fault gouge, *Tectonophysics* **427**(1-4), 231–253.

Pérez-Campos, X., J. McGuire, and G. Beroza (2003). Resolution of the slow earthquake/high apparent stress paradox for oceanic transform fault earthquakes, *J. Geophys. Res. B: Solid Earth* **108**(B9).

Shearer, P. M., G. A. Prieto, and E. Hauksson (2006). Comprehensive analysis of earthquake source spectra in southern California, *J. Geophys. Res. B: Solid Earth* **111**(B6).

Somerville, P. G., N. F. Smith, R. W. Graves, and N. A. Abrahamson (1997). Modification of empirical strong ground motion attenuation relations to include the amplitude and duration effects of rupture directivity, *Seismol. Res. Lett.* **68**(1), 199–222.

Taira, T., R. Bürgmann, R. M. Nadeau, and D. S. Dreger (2014). Variability of fault slip behavior along the San Andreas Fault in the San Juan Bautista Region, *J. Geophys. Res. B: Solid Earth* **119**(12), 8827–8844.

Tan, Y. and D. Helmberger (2010). Rupture directivity characteristics of the 2003 Big Bear sequence, *Bull. Seismol. Soc. Am.* **100**(3), 1089–1106.

Toomey, D. R., R. M. Allen, A. H. Barclay, S. W. Bell, P. D. Bromirski, R. L. Carlson, X. Chen, J. A. Collins, R. P. Dziak, B. Evers, and others (2014). The Cascadia Initiative: A sea change in seismological studies of subduction zones, *Oceanography* **27**(2), 138–150.

Trnkoczy, A. (1999). Topic Understanding and parameter setting of STA/LTA trigger algorithm, *New manual of seismological observatory practice* **2**.

Uchide, T., P. M. Shearer, and K. Imanishi (2014). Stress drop variations among small earthquakes before the 2011 Tohoku-oki, Japan, earthquake and implications for the main shock, *J. Geophys. Res. B: Solid Earth* **119**(9), 7164 – 7174.

Velasco, A. A., C. J. Ammon, and T. Lay (1994). Empirical green function deconvolution of broadband surface waves: Rupture directivity of the 1992 Landers, California (Mw= 7.3), earthquake, *Bull. Seismol. Soc. Am.* **84**(3), 735–750.

Wei, S., D. Helmberger, S. Owen, R. W. Graves, K. W. Hudnut, and E. J. Fielding (2013). Complementary slip distributions of the largest earthquakes in the 2012 Brawley swarm, Imperial Valley, California, *Geophys. Res. Lett.* **40**(5), 847–852.

Wells, D. L. and K. J. Coppersmith (1994). New empirical relationships among magnitude, rupture length, rupture width, rupture area, and surface displacement, *Bull. Seismol. Soc. Am.* **84**(4), 974–1002.

Willoughby, E. C. and R. D. Hyndman (2005). Earthquake rate, slip rate, and the effective seismic thickness for oceanic transform faults of the Juan de Fuca plate system, *Geophys. J. Int.* **160**(3), 855–868.

Withers, M., R. Aster, C. Young, J. Beiriger, M. Harris, S. Moore, and J. Trujillo (1998). A comparison of select trigger algorithms for automated global seismic phase and event detection, *Bull. Seismol. Soc. Am.* **88**(1), 95–106.

Wolfson-Schwehr, M., M. S. Boettcher, J. J. McGuire, and J. A. Collins (2014). The relationship between seismicity and fault structure on the Discovery transform fault, East Pacific Rise, *Geochem. Geophys. Geosyst.* **15**(9), 3698–3712.

Ye, L., T. Lay, K. D. Koper, R. Smalley Jr, L. Rivera, M. G. Bevis, A. F. Zakrajsek, and F. N. Teferle (2014). Complementary slip distributions of the August 4, 2003 Mw 7.6 and November 17, 2013 Mw 7.8 South Scotia Ridge earthquakes, *Earth Planet. Sci. Lett.* **401**, 215–226.

Mailing Addresses

- Joshua R Williams, School of Earth and Environment, University of Leeds, Leeds, UK. LS2 9JT.
- Jessica C Hawthorne, Department of Earth Sciences, University of Oxford, 3 S Parks Rd, Oxford, UK. OX1 3QR.

- Sebastian Rost, School of Earth and Environment, University of Leeds, Leeds, UK. LS2 9JT.
- Tim J Wright, School of Earth and Environment, University of Leeds, Leeds, UK. LS2 9JT.

List of figure captions

Figure 1: (a): Locations and times of M $\geq$ 4.0 earthquakes on the Blanco Fault along profile marker in (c). (b): Position of study area relative to North America. (c): Earthquakes and tectonic structure of the Blanco Fault. The fault trace is marked in red with four bathymetric depressions (BLD, SUD, CAS, GOR) and the Blanco Ridge section of the transform fault (BLR) labeled. The white and black dashed line indicates the profile used for (a) from A to B. The fault structure was taken from Braunmiller and Nábělek (2008). Bathymetry was obtained from ETOPO1 (Amante and Eakins, 2009), and earthquake locations are reported in the NEIC catalog.

Figure 2: Stations used in our analysis. Blue symbols indicate stations that were sometimes excluded to avoid the S wave arrival in our 5-s analysis window. “Other networks” are networks from which we used fewer than 16 stations. Some networks have been grouped for plotting purposes. US states are indicated by the two letter codes. The earthquake catalog from Figure 1 is plotted as translucent circles.

Figure 3: (a): Conceptual diagram of apparent source time function variation by station. The grey circle in the top right is the rupture area of a hypothetical earthquake, with the hypocenter marked by the black circle. The earthquake ruptures outwards from the center, and A and B are asperities within the rupture area which rupture simultaneously but at locations separated by half the rupture diameter D. The apparent source time functions (ASTFs) illustrate the differences in arrival times between signals from A and B. At the western station (W), the signals from A and B are separated in time by $\frac{1}{2}D/V_P$, where V_P is the P-wave velocity. (b): A hypothetical phase coherence spectrum

for this conceptual case. The phase coherence is between the ASTFs at the western and southern stations, and experiences decoherence at a frequency roughly equivalent to $V_P/\frac{1}{2}D$.

Figure 4: An illustration of the phase coherence method using an example earthquake pair. (a) - (d): Aligned traces from an earthquake pair recorded at 4 individual stations. The green window indicates the time window we used to calculate the cross-spectra and phase coherence. (e): Phase of the cross-spectra for each station. Phase spectra are similar in the 1 - 3 Hz band, with the falloff frequency identified from the phase coherence plotted as a dashed black line. (f): Inter-station phase coherence for the four stations in (a) - (d) (red) and all stations recording this event pair (blue with 95% confidence limits shaded), demonstrating the effect of averaging the coherence over stations. Coherence is high in the same frequency band that cross-spectra phases were similar in, resulting in a falloff frequency of roughly 3.4 Hz at a coherence threshold of 0.5. The apparent falloff frequency from the coherence using all stations is similar. Low frequencies have low phase coherence due to energetic low frequency noise in the data set.

Figure 5: Initial unfiltered results for falloff frequency and stress drop variation with magnitude for 161 events. Values on (a) and (b) are colored by number of event pairs available for each event. Note that small magnitude value shifts of less than 0.05 have been applied to differentiate between data points. Body wave magnitudes were translated to moment magnitude using the magnitude relation from Braunmiller and Nábělek (2008). Lower bounds on falloff frequencies have been limited to 1 Hz due to significant low frequency noise, which produces the stepping effect of lower uncertainties on stress drops in (b). The grey shaded area highlights earthquakes with M $<$ 5.0 which are unlikely to have correct falloff frequencies as discussed in the text. The green shaded area indicates falloff frequencies we cannot reliably derive according to the alignment uncertainty, which is discussed in the text. Medians for 0.1 magnitude bins are plotted as squares.

Figure 6: Inter-station phase coherence results for an event with itself, but with varied forced alignment shift. The black line shows maximum phase coherence derived from loop closures only for loops where all 3 events are within 4 km, with the shaded area indicating 95% confidence limits.

Figure 7: Phase coherence spectra for a single event with multiple pairs. The distance between each pair is quoted in the legend, and is estimated using the relative event relocation approach we discussed earlier. The dashed black line is the coherence threshold of 0.5 which we use to pick our falloff frequencies. This figure illustrates that as the distance between events decreases, the falloff frequency increases.

Figure 8: (a): Falloff frequencies obtained from synthetic ruptures for a range of rupture diameters. (b): Histogram of falloff frequencies normalized by V_P/D, where V_P is 8.04 $km\ s^{-1}$, the wavespeed of the upper mantle. The median of the normalized falloff frequencies plots at 1.2, which defines the scaling factor we use in our calculations of the rupture extent.

Figure 9: (a): Falloff frequencies against magnitude for 124 events. (b): Stress drops plotted against magnitude for the same events. Note that magnitudes have been shifted by values less than 0.05 to differentiate between data points. Earthquakes with M $<$ 5.0 which are unlikely to have the correct falloff frequency are highlighted by the grey shaded area on the plot. The 3.7 Hz limit on reliable falloff frequencies due to the alignment uncertainty is indicated by the green shaded area. Results are colored by the number of earthquake pairs available for each measurement. Lower bounds on falloff frequencies have been limited to 1 Hz due to significant low frequency noise. Medians for 0.1 magnitude bins are plotted as squares.

Figure 10: (a): Stress drops for M $\geq$ 5.0 earthquakes on the Blanco Fault plotted along the fault from A to B. The thick black vertical dashed line in the center of the plot indicates cutoff point we defined between the northeast and southwest segments (derived from the Cascadia Depression shown as the red square in (b)). Stress drops are colored

by amplitude. Symbols indicate the number of earthquake pairs that were available for each measurement. The median stress drops for the northwest and southeast segments are shown by the dashed horizontal green and black lines, respectively. The shaded areas around these medians show the 95% confidence limits. (b): Stress drops for M $\geq$ 5.0 earthquakes on the Blanco Fault plotted in map view.

Figures

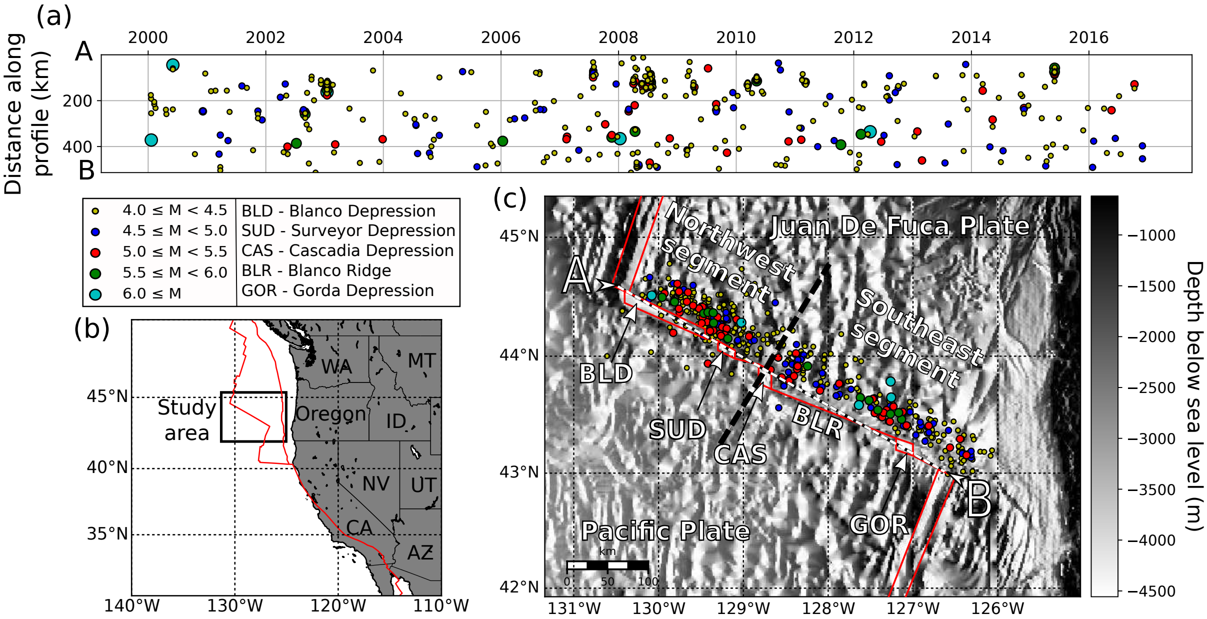

Figure 1: (a): Locations and times of M $\geq$ 4.0 earthquakes on the Blanco Fault along profile marker in (c). (b): Position of study area relative to North America. (c): Earthquakes and tectonic structure of the Blanco Fault. The fault trace is marked in red with four bathymetric depressions (BLD, SUD, CAS, GOR) and the Blanco Ridge section of the transform fault (BLR) labeled. The white and black dashed line indicates the profile used for (a) from A to B. The fault structure was taken from Braunmiller and Nábělek (2008). Bathymetry was obtained from ETOPO1 (Amante and Eakins, 2009), and earthquake locations are reported in the NEIC catalog.

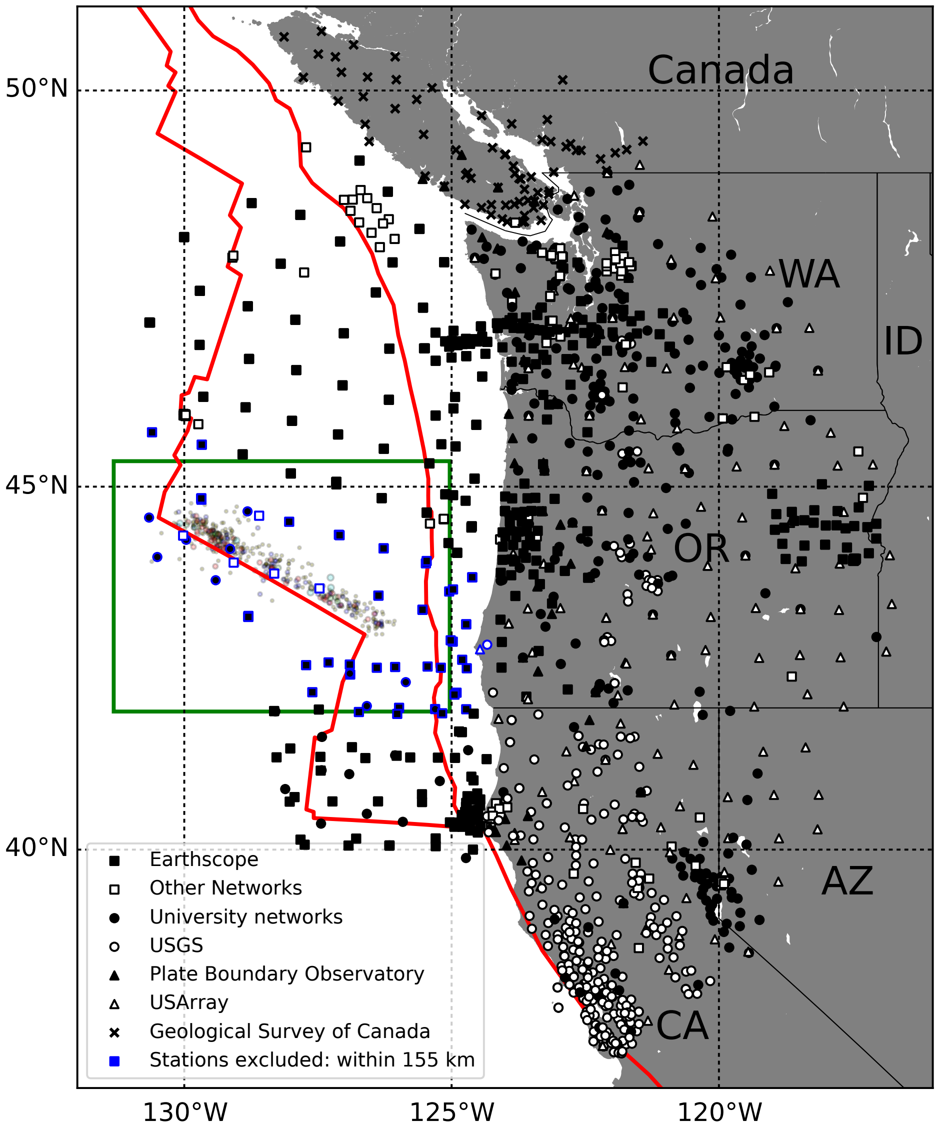

Figure 2: Stations used in our analysis. Blue symbols indicate stations that were sometimes excluded to avoid the S wave arrival in our 5-s analysis window. "Other networks" are networks from which we used fewer than 16 stations. Some networks have been grouped for plotting purposes. US states are indicated by the two letter codes. The earthquake catalog from Figure 1 is plotted as translucent circles.

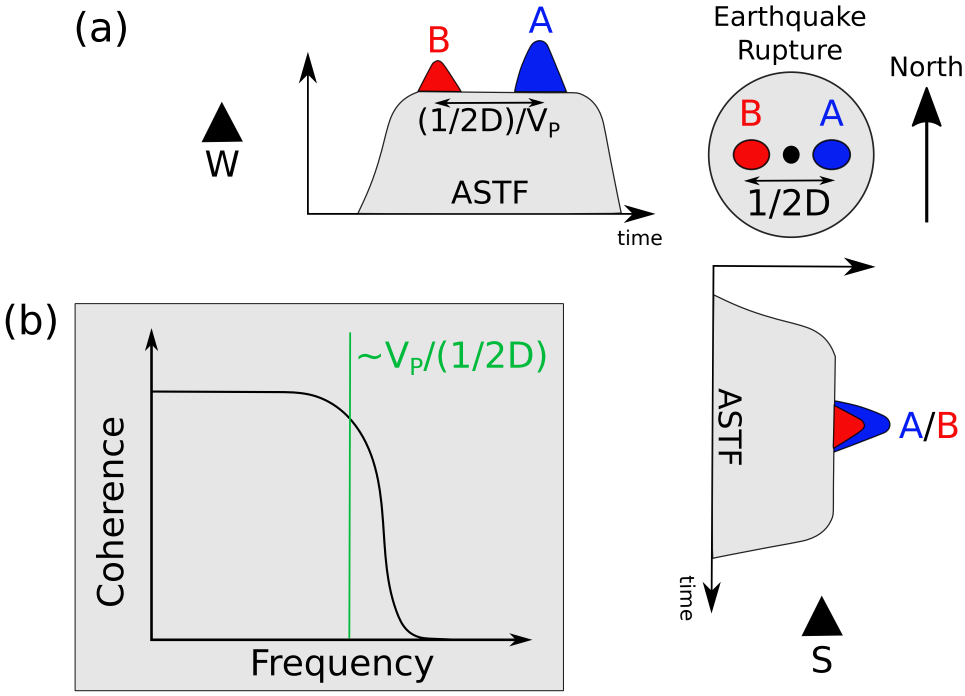

Figure 3: (a): Conceptual diagram of apparent source time function variation by station. The grey circle in the top right is the rupture area of a hypothetical earthquake, with the hypocenter marked by the black circle. The earthquake ruptures outwards from the center, and A and B are asperities within the rupture area which rupture simultaneously but at locations separated by half the rupture diameter D. The apparent source time functions (ASTFs) illustrate the differences in arrival times between signals from A and B. At the western station (W), the signals from A and B are separated in time by $\frac{1}{2}D/V_P$, where V_P is the P-wave velocity. (b): A hypothetical phase coherence spectrum for this conceptual case. The phase coherence is between the ASTFs at the western and southern stations, and experiences decoherence at a frequency roughly equivalent to $V_P/\frac{1}{2}D$.

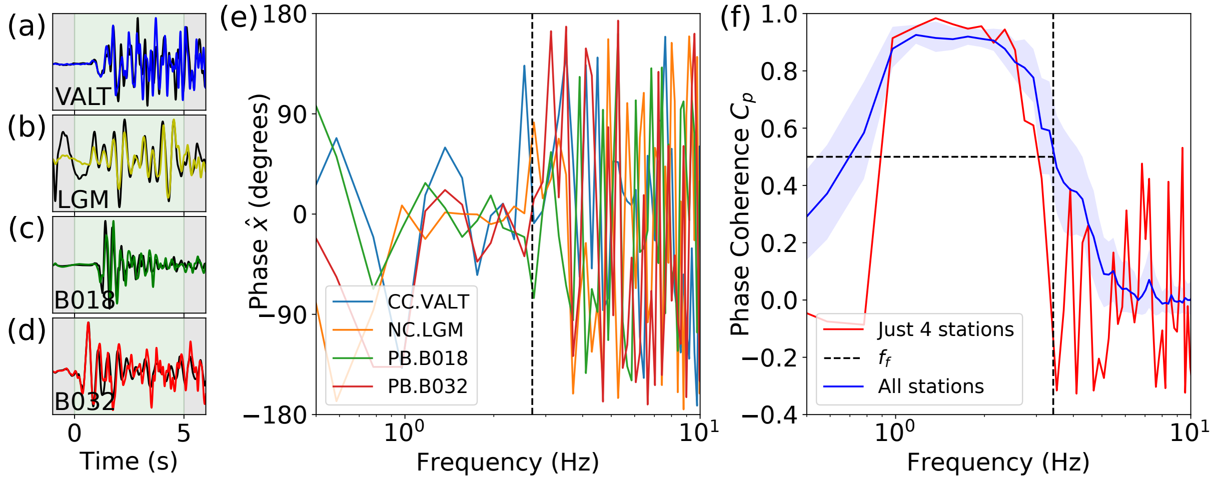

Figure 4: An illustration of the phase coherence method using an example earthquake pair. (a) - (d): Aligned traces from an earthquake pair recorded at 4 individual stations. The green window indicates the time window we used to calculate the cross-spectra and phase coherence. (e): Phase of the cross-spectra for each station. Phase spectra are similar in the 1 - 3 Hz band, with the falloff frequency identified from the phase coherence plotted as a dashed black line. (f): Inter-station phase coherence for the four stations in (a) - (d) (red) and all stations recording this event pair (blue with 95% confidence limits shaded), demonstrating the effect of averaging the coherence over stations. Coherence is high in the same frequency band that cross-spectra phases were similar in, resulting in a falloff frequency of roughly 3.4 Hz at a coherence threshold of 0.5. The apparent falloff frequency from the coherence using all stations is similar. Low frequencies have low phase coherence due to energetic low frequency noise in the data set.

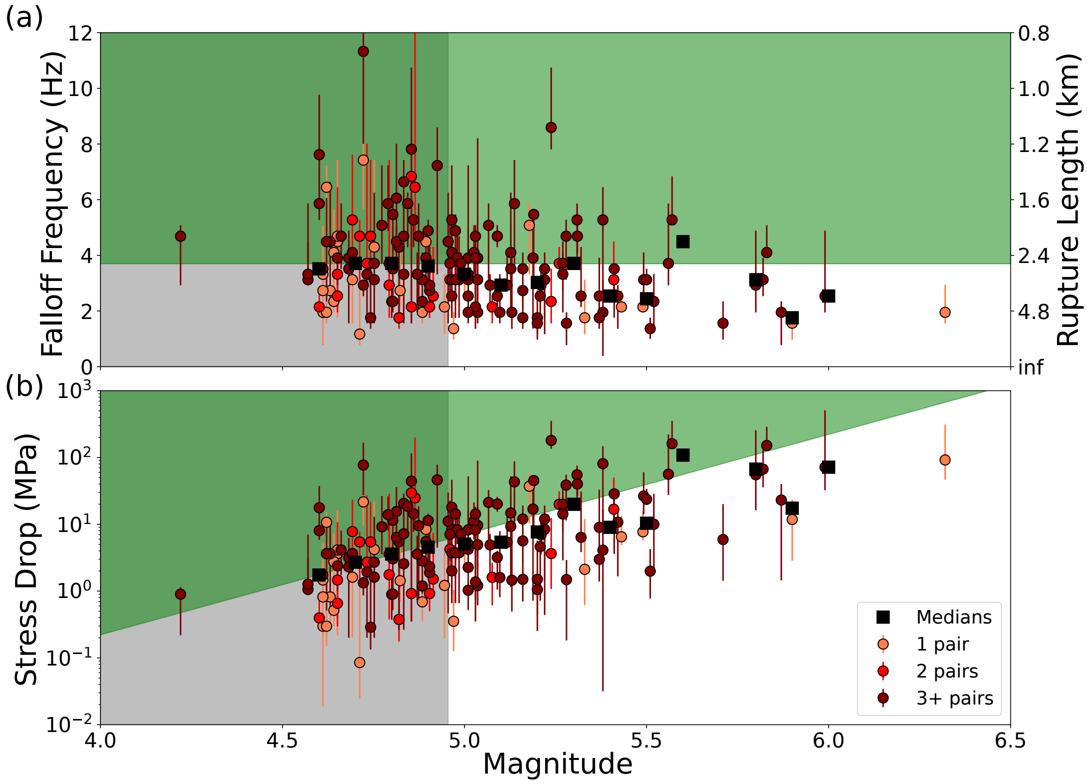

Figure 5: Initial unfiltered results for falloff frequency and stress drop variation with magnitude for 161 events. Values on (a) and (b) are colored by number of event pairs available for each event. Note that small magnitude value shifts of less than 0.05 have been applied to differentiate between data points. Body wave magnitudes were translated to moment magnitude using the magnitude relation from Braunmiller and Nábělek (2008). Lower bounds on falloff frequencies have been limited to 1 Hz due to significant low frequency noise, which produces the stepping effect of lower uncertainties on stress drops in (b). The grey shaded area highlights earthquakes with M < 5.0 which are unlikely to have correct falloff frequencies as discussed in the text. The green shaded area indicates falloff frequencies we cannot reliably derive according to the alignment uncertainty, which is discussed in the text. Medians for 0.1 magnitude bins are plotted as squares.

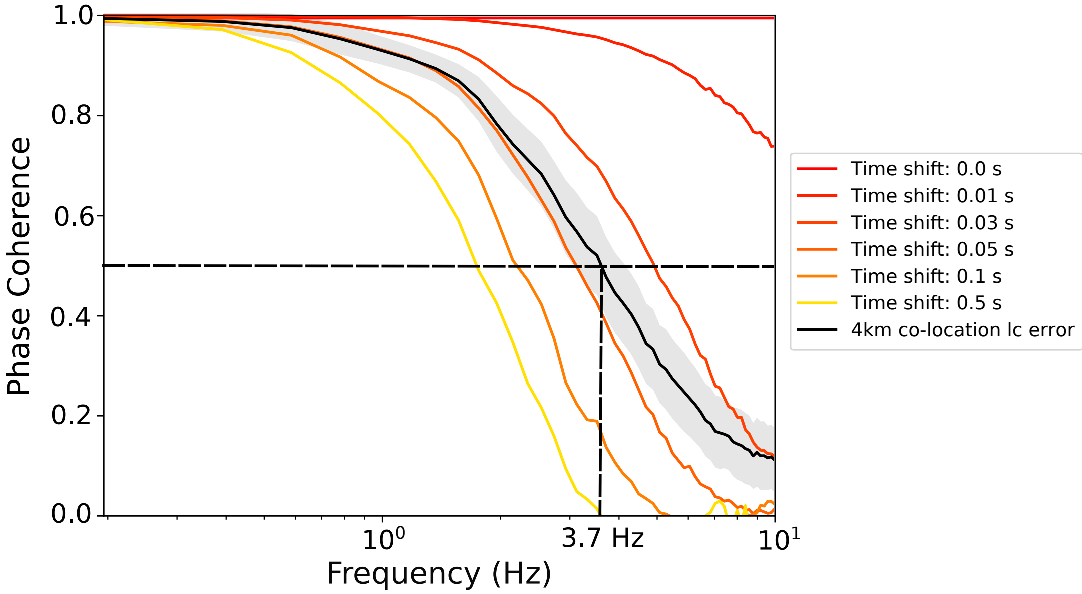

Figure 6: Inter-station phase coherence results for an event with itself, but with varied forced alignment shift. The black line shows maximum phase coherence derived from loop closures only for loops where all 3 events are within 4 km, with the shaded area indicating 95% confidence limits.

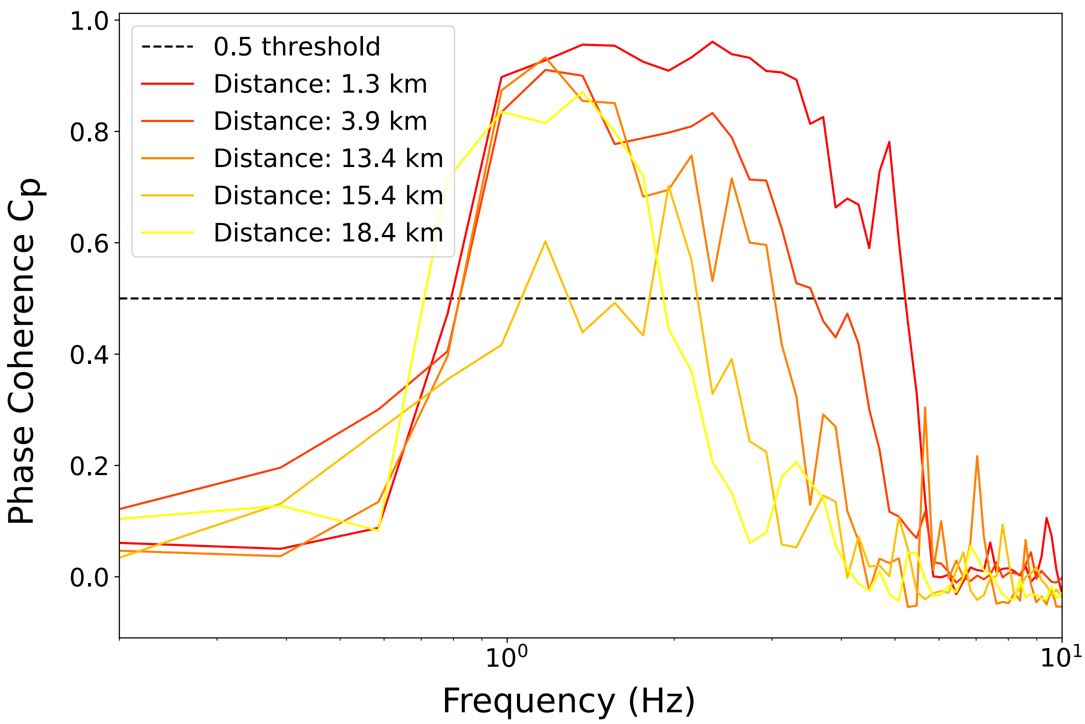

Figure 7: Phase coherence spectra for a single event with multiple pairs. The distance between each pair is quoted in the legend, and is estimated using the relative event relocation approach we discussed earlier. The dashed black line is the coherence threshold of 0.5 which we use to pick our falloff frequencies. This figure illustrates that as the distance between events decreases, the falloff frequency increases.

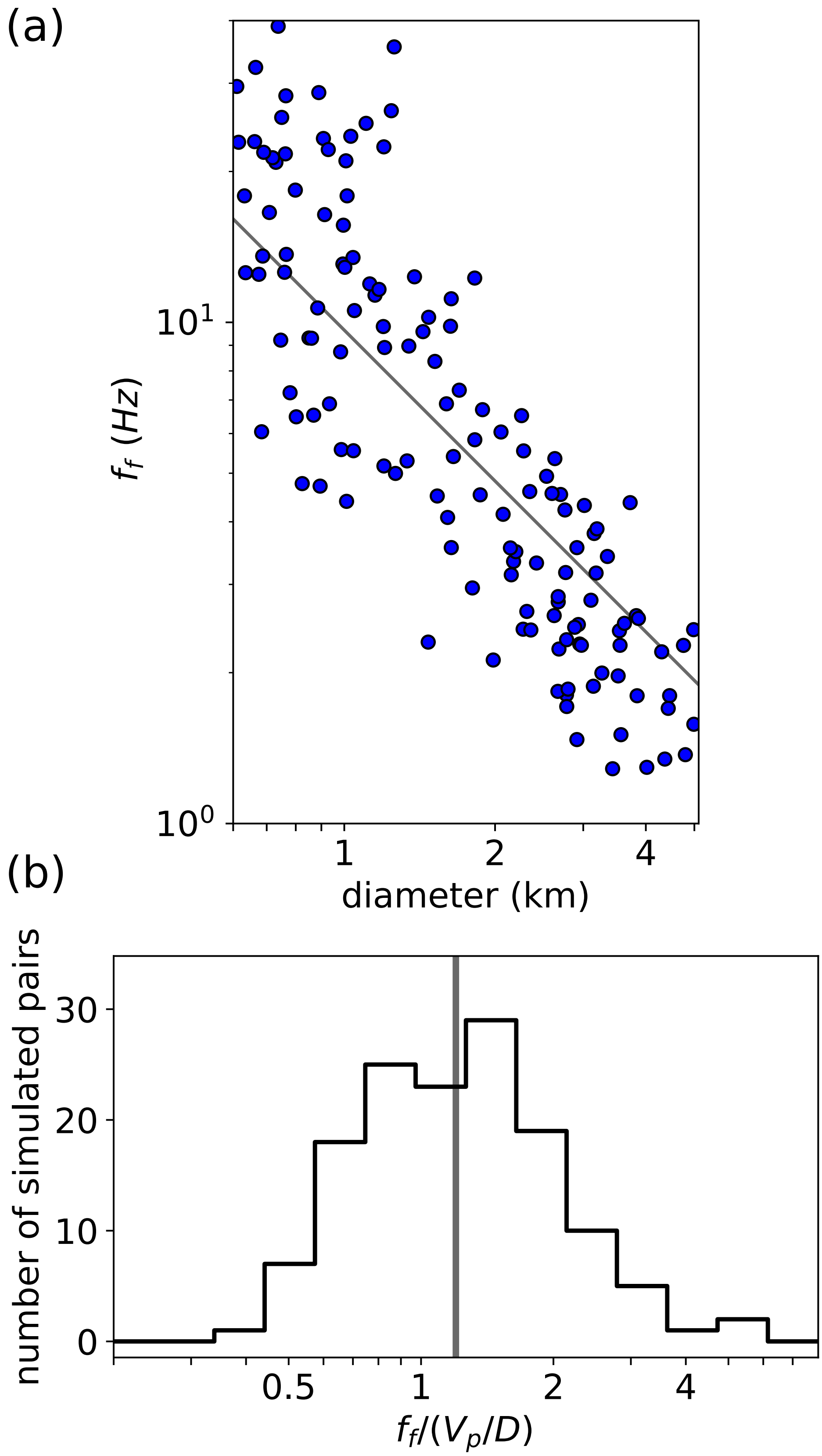

Figure 8: (a): Falloff frequencies obtained from synthetic ruptures for a range of rupture diameters. (b): Histogram of falloff frequencies normalized by V_P/D, where V_P is 8.04 $km\ s^{-1}$, the wavespeed of the upper mantle. The median of the normalized falloff frequencies plots at 1.2, which defines the scaling factor we use in our calculations of the rupture extent.

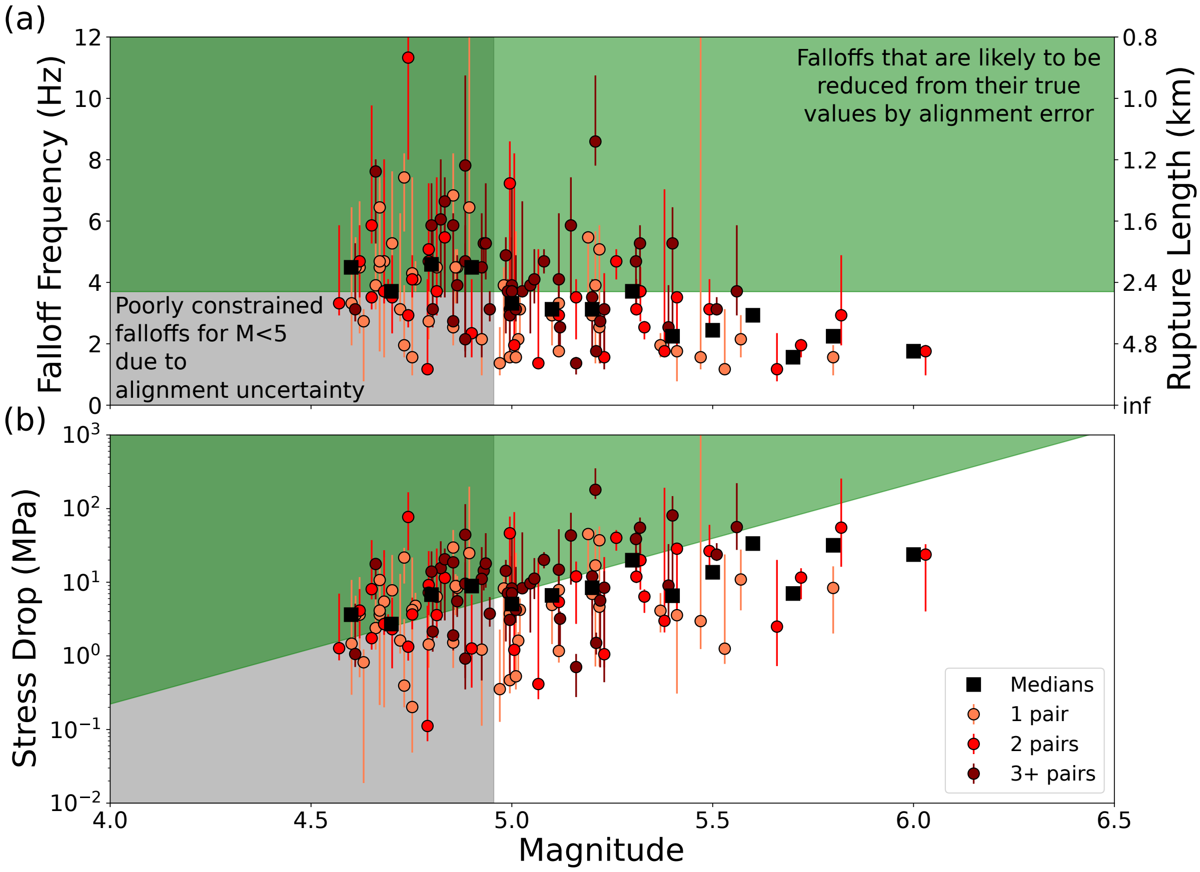

Figure 9: (a): Falloff frequencies against magnitude for 124 events. (b): Stress drops plotted against magnitude for the same events. Note that magnitudes have been shifted by values less than 0.05 to differentiate between data points. Earthquakes with M < 5.0 which are unlikely to have the correct falloff frequency are highlighted by the grey shaded area on the plot. The 3.7 Hz limit on reliable falloff frequencies due to the alignment uncertainty is indicated by the green shaded area. Results are colored by the number of earthquake pairs available for each measurement. Lower bounds on falloff frequencies have been limited to 1 Hz due to significant low frequency noise. Medians for 0.1 magnitude bins are plotted as squares.

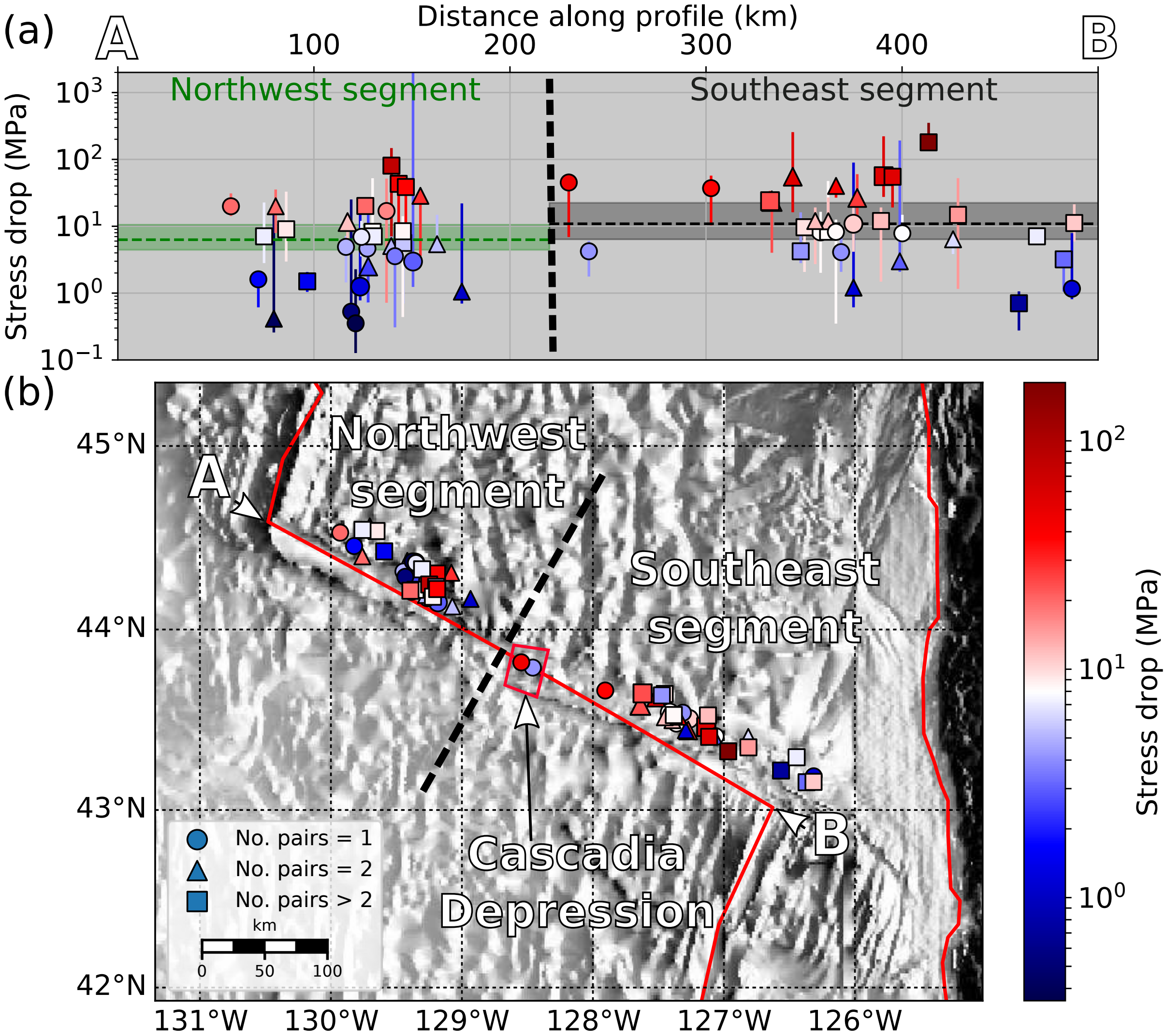

Figure 10: (a): Stress drops for M ≥ 5.0 earthquakes on the Blanco Fault plotted along the fault from A to B. The thick black vertical dashed line in the center of the plot indicates cutoff point we defined between the northeast and southwest segments (derived from the Cascadia Depression shown as the red square in (b)). Stress drops are colored by amplitude. Symbols indicate the number of earthquake pairs that were available for each measurement. The median stress drops for the northwest and southeast segments are shown by the dashed horizontal green and black lines, respectively. The shaded areas around these medians show the 95% confidence limits. (b): Stress drops for M ≥ 5.0 earthquakes on the Blanco Fault plotted in map view.